



Development of a Highly-Sensitive Diamond-Based Magnetometer

Author: Jelle Vodnik

Supervisors:

Prof. Dr. Milos Nesladek, Drs. Ing. Jaroslav Hruba, dr. Emilie Bourgeois

Bachelor project

Academical year 2015 - 2016

Contents

1 Abstract	2
2 Introduction	3
3 Theory	4
3.1 The Atomic Structure	4
3.2 The Electronic Structure	5
3.3 Applying a Magnetic Field	7
3.4 The Total Ground State Hamiltonian	7
4 Magnetometry: the Principle	10
4.1 Optically Detected Magnetic Resonance	10
4.2 Magnetic Field Sensitivity of ODMR	11
4.3 Photo-current Detected Magnetic Resonance	12
5 Magnetometry: the Development	13
5.1 Development of the ODMR Magnetometer: Part 1	13
5.2 Development of the ODMR Magnetometer: Part 2	19
5.3 Development of the PDMR Magnetometer	23
6 Results and Discussion	24
6.1 ODMR Magnetometer: Part 1	24
6.2 ODMR Magnetometer: Part 2	25
6.3 PDMR Magnetometer	27
7 Conclusion and a Look Forward	29
8 Acknowledgements	30
9 References	31
10 Appendices	33
10.1 Appendix A: Optical Setup with Specifications	33
10.2 Appendix B: Arduino Test Code	34
10.3 Appendix C: Linearity of the PDMR Measurements	37
10.4 Appendix D: Magnetic Field Strength of the Spherical Magnet	38

1 Abstract

The spin-selective readout of the negatively charged nitrogen vacancy (NV) centre in diamonds gives a highly sensitive and stable way of detecting magnetic fields. The objective of this thesis is to develop a prototype magnetometer which will be accommodated on board of a stratospheric balloon provided by the European Space Agency (ESA) to a team of students from the university of Hasselt for the OSCAR (Optical Sensors based on CArbon materials) project. The main focus of the magnetometer component of project OSCAR is to verify the functionality in harsh near-space environments, such as elevated radiation levels, vacuum and low temperature. If proven to be successful, this may lead to further development of applications for aerospace engineering.

The presented work gives an introduction to the general principles of the NV defect, the different positions it can assume within the crystal lattice and the electronic structure of the NV centre. Methods used for reconstruction of the magnetic field vector based on the signals obtained from NV defects are explained in terms of calculations of the change in energy of the states of the electronic structure, caused by the influence of external magnetic fields on the NV centre. This is used as a suitable model for magnetic field measurements using the NV diamond centre.

The principle is explained showing how the previous electronic structure can be used to give a magnetic field readout, by using an optical setup for a method called optically detected magnetic resonance (ODMR). It is explained why the sensitivity is dependent on applied laser power and microwave power, but also on the purity of the diamond. A novel readout approach for the detection of magnetic fields, called photo-current detected magnetic resonance (PDMR), is introduced. This method is based on the electrical readout of the signal created by the NV defects, which in comparison to ODMR does not require a complex optical setup and bulky detectors. This results in the reduction of the overall size of the device and its possible integration on a chip.

2 Introduction

Magnetic field sensing is a widespread technology with practical use in various fields. The magnetometers can be found not only in commonly known applications such as in navigation, geology, mineral exploration and archaeology. But also in the cutting edge technologies like satellite positioning, weather prediction, biomedical applications and potentially in quantum technologies. The current methods for magnetic sensing are limited either by their low sensitivity (GMR) [2] or by their operational temperature (SQUID) [1]. Therefore, we focus on a novel type of magnetometers based on diamond. The diamond is not only a stable material in various environments, it also contains opto-magnetic defects in its structural lattice know as Nitrogen-Vacancy (NV) centres. The negatively charged NV centres provide a stable method for magnetic field sensing, working at room temperatures on a nanometre scale with sub-picotesla resolution [3]. This makes diamond NV centres a promising new tool, suitable for all kinds of applications in various environments.

One of the benefits of the diamond is the wide band gap. This results in high radiation hardness of the material which is ideal for space applications. In order to verify the principle in space-like conditions, participation was requested and granted for the BEXUS (Balloon Experiments for University Students) project organised by European Space Agency (ESA). For the purpose of this project a magnetometer prototype is developed based on the NV defect diamond, which will be sent on board of a balloon into the stratosphere. The goal is to observe the influence of the harsh near-space conditions and unpredictable behaviour in the measurements.

NV defects in diamonds are impurities in a diamond lattice where two carbon atoms have been replaced by a nitrogen atom and a vacancy. The defects have two known charge states, NV^0 and NV^- . Their electronic structure is characterised by the spin-sensitive photo-luminescence emitted by an electron during its relaxation from the excited to the ground state. For magnetometer applications this effect can be exploited as the change in energy levels of the centre changes linearly with the magnetic field strength.

The aim of this thesis is to develop a compact prototype magnetometric device based on diamond NV centres which will eventually be placed on board of a stratospheric balloon in order to verify the principles and stability of the proposed method in harsh environmental conditions.

3 Theory

3.1 The Atomic Structure

The Nitrogen Vacancy centre in a diamond is a defect where two carbon atoms are replaced by a nitrogen atom and an adjacent vacancy. The NV centre is sensitive only to the magnetic fields oriented or projected along the NV axis [6]. This axis is the spatial axis from the vacancy towards the nitrogen. Therefore the orientation of the NV centre in diamond lattice is important especially for vector magnetometry. There are four possible orientations for the NV defects in the diamond, corresponding to the location of the nitrogen atom with respect to the vacancy. These possible directions are $[1\ 1\ 1]$, $[\bar{1}\ 1\ 1]$, $[1\ \bar{1}\ \bar{1}]$ or $[\bar{1}\ \bar{1}\ \bar{1}]$. The bar over the index indicates the negative index. The $[1\ 1\ 1]$ crystal lattice orientation is seen in figure 1a. The possible orientations can be seen in figure 1b.

The structure has been observed in two different stable forms; a neutral NV^0 and a negative NV^- . The NV^0 centre consists of three electrons from the dangling bonds between the vacancy and three carbon atoms. Two more electrons come from the dangling bond between the nitrogen and the vacancy. The negatively charged NV^- centre has one extra electron donated from the bulk of the diamond [4] [19].

Due to the energy structure of the NV^- centre's ground state (a spin triplet), it is useful for sensing applications. Experiments have shown that the NV^0 defects are not usable for magnetometer applications [3] [16]. In the following parts the NV^- centre will be referred to as the NV centre.

For the purpose of magnetometry, it is important to know the orientation of the NV centre. The four different directions will produce four sets of resonance peaks in the microwave frequency spectrum when applying an external magnetic field, as the magnetic field is projected to each NV orientation with a different magnitude [3] [5] [6].

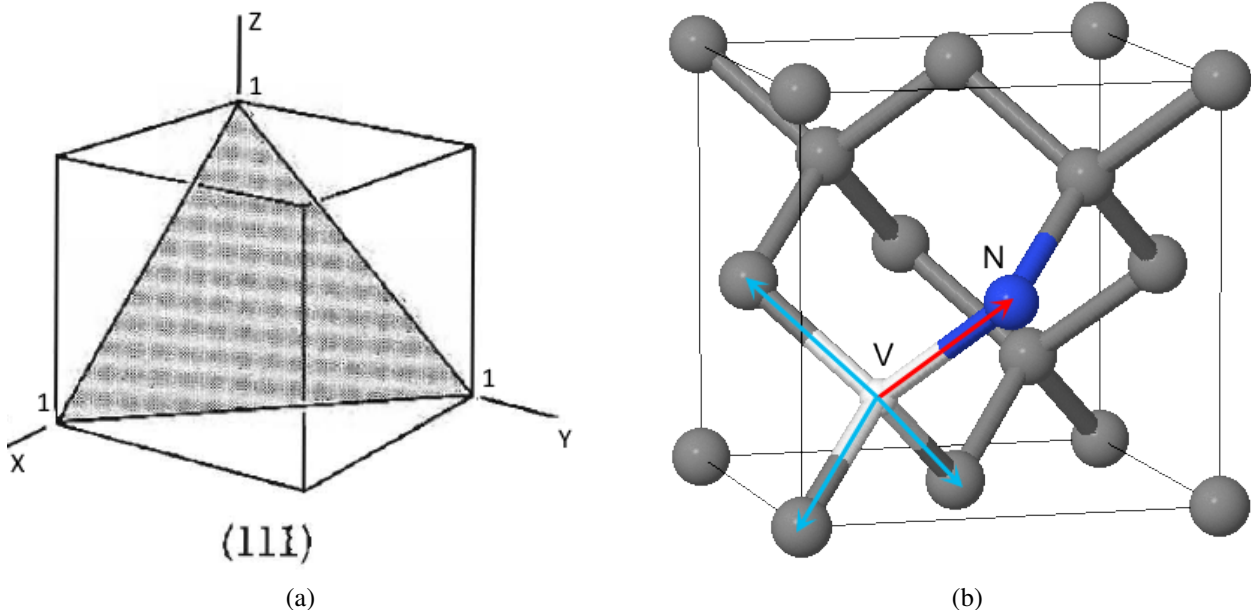


Figure 1: (a) Orientation of the $[1\ 1\ 1]$ plane [2]. (b) Atomic structure of the nitrogen vacancy defect in the $[1\ 1\ 1]$ orientation. In red: the NV axis in this particular diamond unit cell. In blue: the other possible axes.

3.2 The Electronic Structure

The NV defect has a triplet ground state called 3A_2 and a triplet excited state 3E [10]. This is caused by the defect having a spin of $S = 1$, because two of the six involved electrons are unpaired. Both add $\frac{1}{2}$ to the total spin. The degeneracy of the triplet ground state is lifted by spin-spin interaction which causes there to be a singlet $|0\rangle$ and doublet $| -1 \rangle$ and $| +1 \rangle$ at a slightly higher energy. These states indicate m_s , the spin projection along the axis of the NV defect. This effect also causes the excited state to lift the degeneracy, but this state is also influenced by second order effects which come from spin-orbit coupling. The second order effects don't affect the ground state triplet [7] [19]. A representation of this structure can be seen in figure 3a. Two metastable states are also seen in this structure. A transition between these will give emission in the infrared spectrum.

The resonant transition between the $|0\rangle$ ground state and the $|0\rangle$ excited state occurs at 1,945 eV, which corresponds to a wavelength of 637 nm. As seen in figure 2, the absorption spectrum of the defect lies between 450 and 650 nm. Ground state to excited state transition is spin-conserving, although different phonon modes are able to be reached. This is why the absorption spectrum is so wide. The same thing is happening to the emission spectrum of the NV defect. This spectrum lies between 625 and 800 nm. Electrons excited from the $| -1 \rangle$ and $| +1 \rangle$ to the excited state have a higher chance to de-excite via the metastable states, which corresponds to a decrease in intensity of the emitted fluorescent light. This path is called inter-system crossing [4]. The process of measuring the intensity of the emitted light is called optically detected magnetic resonance (ODMR).

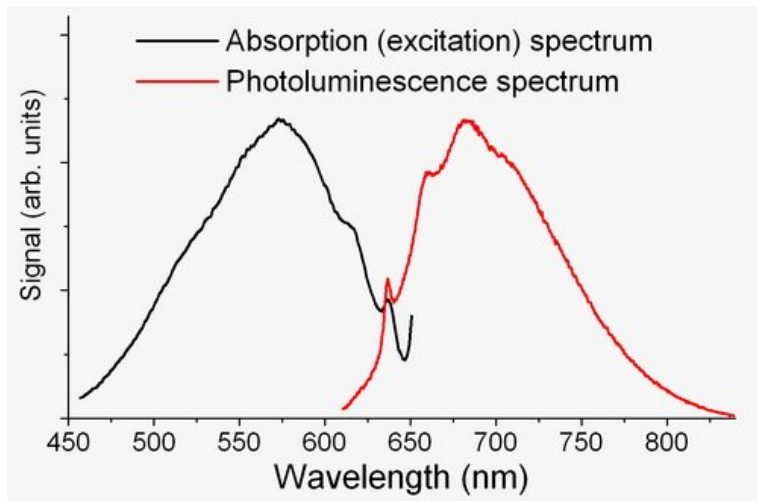
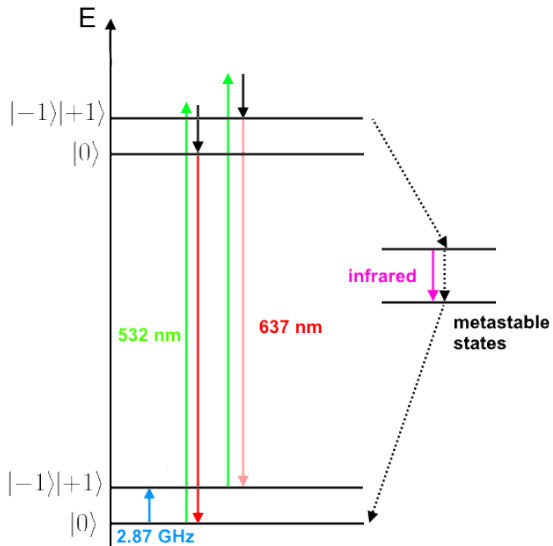


Figure 2: Absorption and emission spectrum of the NV defect diamond [24].

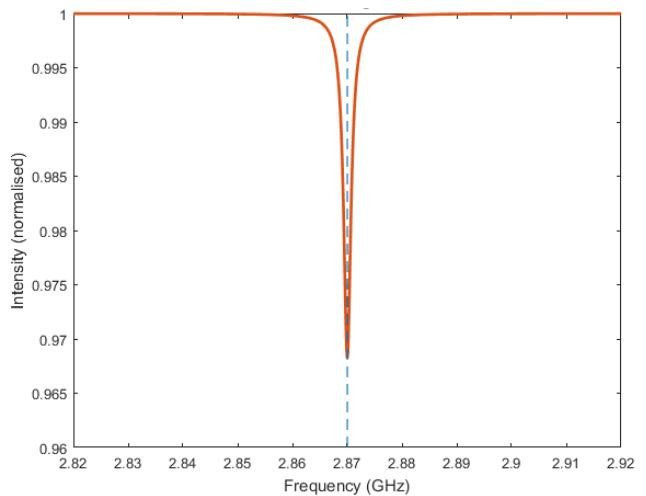
In the absence of an external magnetic field, the frequency transition between the doublet and the singlet ground states is 2,87 GHz [9]. This effect is known as the zero-field splitting. The same effect is observed with 3E . The corresponding zero-field splitting is located at 1,42 GHz due to the contribution of spin-orbit coupling [20].

When applying a microwave frequency sweep to the diamond before exciting the electrons to the excited 3E state, a minimum will show up at the resonant frequency of 2,87 GHz. Around this resonant frequency the electrons will be raised to the $| -1 \rangle$ and $| +1 \rangle$ ground states, which means they will have a higher chance to pass the metastable states. A representative frequency sweep can be seen in figure 3b.

This effect can be utilised for magnetic field sensing applications. Next section will show that the $| -1 \rangle$ and $| +1 \rangle$ states will split due to an applied magnetic field. This splitting will be linearly proportional to the strength of the magnetic field (for small fields) and is called Zeeman splitting.



(a)



(b)

Figure 3: (a) Electronic structure of a negative nitrogen-vacancy defect in diamond. Electrons are excited by a 532 nm laser and emit fluorescent light when relaxing back to the ground state. (b) Spectrum of a nitrogen-vacancy defect. When applying a microwave frequency sweep, the resonant frequency (zero-field splitting) can be observed.

3.3 Applying a Magnetic Field

When applying a magnetic field, the degeneracy of the ground states $| -1 \rangle$ and $| +1 \rangle$ is lifted. Instead of a resonance at the zero-field splitting frequency, two resonant frequencies are now observed. The frequency shift is proportional to the magnetic field strength, linearly proportional if the magnetic field strength is significantly smaller than 100 mT [3] [16]. The linear splitting increases by 28 MHz per mT in the case of small magnetic fields [17]. The effect of a magnetic field on the electronic structure can be seen in figure 4a, while a representative frequency sweep can be seen in figure 4b.

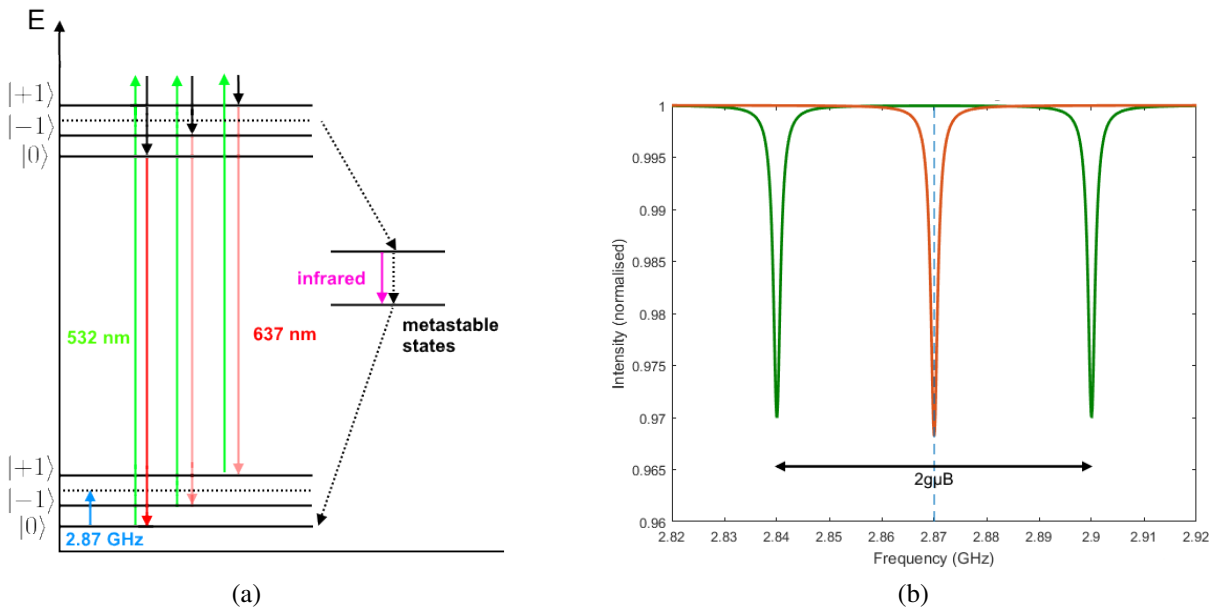


Figure 4: (a) Electronic structure of a negative nitrogen-vacancy defect in diamond after applying a magnetic field. The ground state doublet splits. (b) Spectrum of a nitrogen-vacancy defect with (green) and without (orange) applying a magnetic field. By applying a frequency sweep, the resonant frequencies can be observed. Here this involves both the zero-field splitting and the Zeeman splitting. In the following section the formula will be explained.

3.4 The Total Ground State Hamiltonian

The ground-state spin Hamiltonian can be split up into two terms: the first part considers the effects caused by fine structure and is given in equation 1. The second term gives the hyperfine structure effects and is given in equation 2.

$$(1) \quad H_{fs} = D(S_z^2 - \frac{1}{3}S(S+1)) + E(S_x^2 - S_y^2) + g_e\mu_b\vec{B} \cdot \vec{S}$$

The first term on the right gives the zero-field splitting. This is caused by the interaction of the electron spin with the crystal field. The second term gives the effect of strain caused by an applied electric field or mechanical force. The third term gives the Zeeman splitting. D (2,87 GHz) and E (kHz - MHz range) are the fine structure parameters, g_e is the g-factor of the electron spin and has value 2,0023, μ_b is the Bohr magneton and S_x , S_y and S_z are the Pauli matrices for spin $S = 1$.

$$S_x = \frac{\hbar}{\sqrt{2}} \begin{pmatrix} 0 & 1 & 0 \\ 1 & 0 & 1 \\ 0 & 1 & 0 \end{pmatrix}, S_y = \frac{\hbar}{\sqrt{2}} \begin{pmatrix} 0 & -i & 0 \\ -i & 0 & i \\ 0 & i & 0 \end{pmatrix}, S_z = \hbar \begin{pmatrix} 1 & 0 & 0 \\ 0 & 0 & 0 \\ 0 & 0 & -1 \end{pmatrix}$$

Vectors \vec{B} and \vec{S} are $[B_x, B_y, B_z]$ and $[S_x, S_y, S_z]$ respectively [3] [4] [9] [12].

The hyperfine Hamiltonian [4] [5] [9]:

$$(2) \quad H_{hfs} = P(\hat{I}_z^2 - \frac{1}{3}I(I+1)) + A_{par}S_zI_z + A_{perp}(S_xI_x + S_yI_y) + g_N\mu_N\vec{I}\cdot\vec{B}$$

The first term on the right represents the nuclear electric quadrupole, where P has value $-4,95$ MHz. The second and third term give the hyperfine coupling of the nitrogen nucleus. Here A_{par} and A_{perp} are the hyperfine coupling parameters. Both lie in the range of a few MHz. The last term gives the nuclear Zeeman splitting, with $g_N = 0,403$ the nuclear-spin g-factor, μ_N the nuclear magneton coefficient and \vec{I} the nuclear spin vector, with components $[I_x, I_y, I_z]$.

Ignoring the hyperfine effects and the constant term, $\frac{2}{3}$, in the first term of the fine structure (to show the effect while keeping the eigenvalues of the total Hamiltonian simple), the spectrum of the microwave sweep will have eight peaks, four sets of two, for the four mentioned NV axes. Filling in the Pauli matrices into equation 1 and squaring them will give:

$$H = \hbar^2 \begin{pmatrix} D & 0 & 0 \\ 0 & 0 & 0 \\ 0 & 0 & D \end{pmatrix} + \frac{\hbar^2}{2} \begin{pmatrix} 0 & 0 & 2E \\ 0 & 0 & 0 \\ 2E & 0 & 0 \end{pmatrix} + g_e\mu_b \begin{pmatrix} B_z & \frac{1}{\sqrt{2}}(Bx+iBy) & 0 \\ \frac{1}{\sqrt{2}}(Bx-iBy) & 0 & \frac{1}{\sqrt{2}}(Bx+iBy) \\ 0 & \frac{1}{\sqrt{2}}(Bx-iBy) & -B_z \end{pmatrix}$$

Diagonalising and taking an easy field as an illustration, for example $B = [0,0, B_0]$ gives eigenvalues $0, D - \sqrt{E^2 + (g_e\mu_b B_0)^2}$ and $D + \sqrt{E^2 + (g_e\mu_b B_0)^2}$. The latter two give the splitting due to the magnetic field. The calculation involves only the ground state and the E parameter is essentially zero in the ground-state spin Hamiltonian [5] [21]. Therefore, the second term in equation 1 can be neglected. A visualisation of the eight peaks can be seen in figure 5, when putting back $\frac{2}{3}$ into the fine structure Hamiltonian.

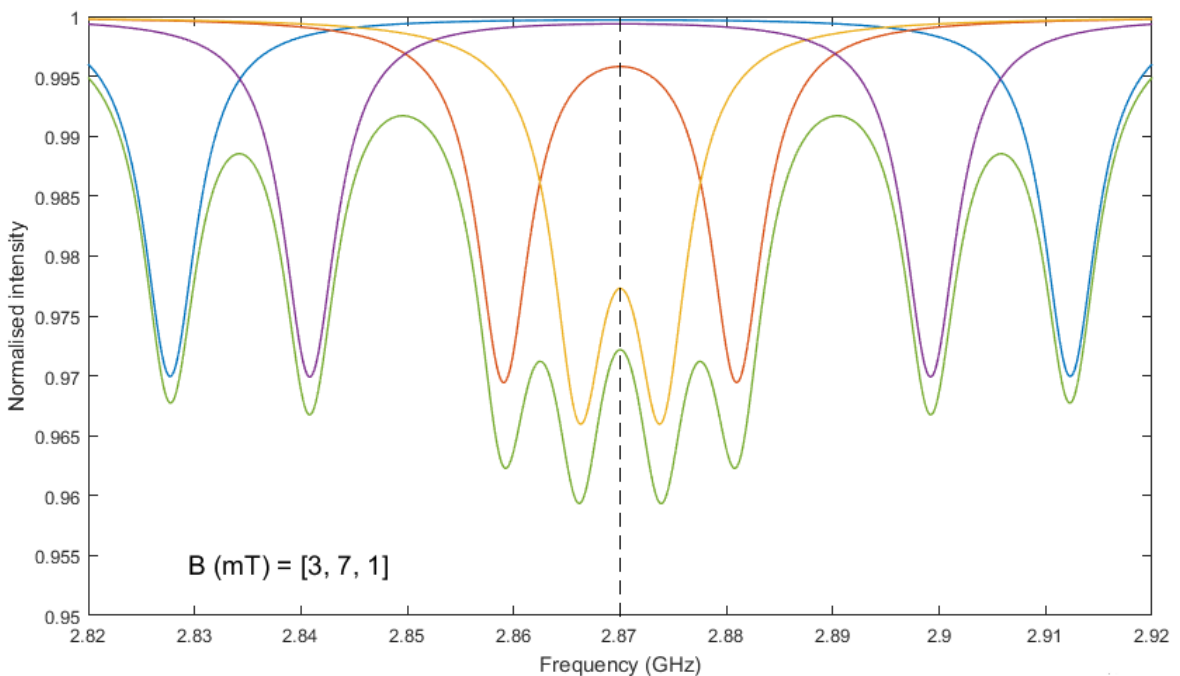


Figure 5: A visualisation of the Zeeman splitting for the four possible directions of the NV axis. The direction of the applied magnetic field (in mT) is $[3 \ 7 \ 1]$. In green: the sum of all the peaks.

The previous model is an approximation in case no electric and strain fields are applied and the magnetic field is much lower than 100 mT. The energy shift is linearly dependent on the strength of the magnetic field. This model is sufficient for the scope of this thesis, since the goal is to measure magnetic fields below 100 mT.

4 Magnetometry: the Principle

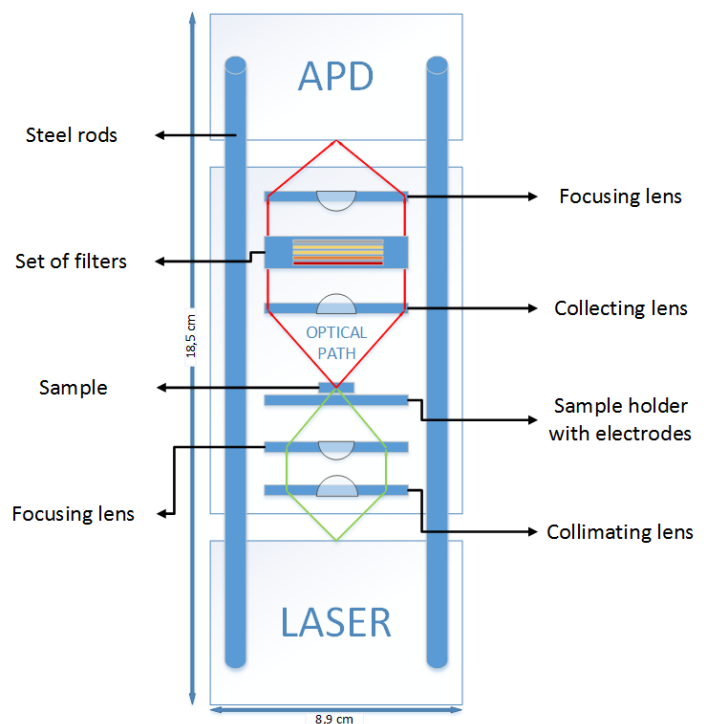
4.1 Optically Detected Magnetic Resonance

In section 3.2 the electronic structure of the defect was explained. The setup for optically detected magnetic resonance (ODMR) is shown in figure 6a. A schematic is given in figure 6b.

The excitation of the electrons in the ground state 3A_2 to the excited state is done by a green laser (532 nm). The laser beam produced by a laser diode is collimated by a collimating lens. A focusing lens focuses the beam on the diamond sample. At the same time microwave frequencies are applied to the sample to excite the electrons from $|0\rangle$ to the $|-\rangle$ and $|+\rangle$ states. The emission light from the diamond is collected by a collecting lens and passes through a set of filters to attenuate and filter out the unwanted wavelengths. The filtered light is then focused on the active area of the avalanche photo diode (APD) by a focusing lens. The APD's signal is then plotted versus the applied frequency on the sample.



(a)



(b)

Figure 6: (a) Setup for ODMR. At the top the APD can be seen, at the bottom the laser diode is mounted and in between are the optomechanics with the sample. (b) Simple schematic of the setup showing all the relevant components.

4.2 Magnetic Field Sensitivity of ODMR

The sensitivity is limited by the quantum noise, in particular the photon shot noise. This shot noise is a consequence of the photons being discrete. At low intensities, the incoming photon flux varies at different places on a detector. The photon shot noise has a standard deviation of $\sqrt{I\Delta t}$, where Δt is the measurement time and I is the incoming intensity [15].

The magnetic field sensitivity limited by the shot noise for a single NV centre is given by equation 3 [3] [14] [11].

$$(3) \quad \eta = \delta B \sqrt{\Delta t} \approx \frac{h}{g\mu_b} \frac{\Delta\nu}{C\sqrt{I_0}}$$

Where C is the contrast (normalised intensity difference between the intensity at the resonant frequency (dip) and at a non-resonant frequency), $\Delta\nu$ is the line width of the resonance peaks, δB is an infinitesimal magnetic field change and I_0 is the NV defect photo-luminescence rate. When using an ensemble of NV centres (with N number of centres), the sensitivity is improved by a factor $\frac{1}{\sqrt{N}}$ [3]. But due to the aforementioned fact that a [111] NV defect diamond has four possible orientations, the reduction factor is compensated.

The limit to the ODMR line width is related to the inhomogeneous dephasing time of the NV defect electron spin, T_2^* , by $\Delta\nu \sim \frac{1}{T_2^*}$. T_2^* can be seen as the time it takes for the coherence between the electron spins to decay. Considering the applied microwaves and the laser power induce power broadening of the line width, this limit is hard to achieve. T_2^* is mainly related to paramagnetic impurities [4] and can be increased by producing an ultra-pure NV defect diamond. The line width $\Delta\nu$ can be made narrower by reducing either the laser power or the power of the applied microwaves. By reducing the latter, the amount of electrons going to the $| -1 \rangle$ and $| +1 \rangle$ ground states will also be reduced. This will in turn reduce the contrast. Reducing the laser power will result in a decrease of contrast. On the contrary, applying a too high power will increase the noise on the spectrum. At a certain laser power saturation of the amount of the excited electrons occurs. An optimal laser power has to be found [18].

The decrease of the line width can be performed without reducing the laser or microwave powers. By applying a Ramsey $\frac{\pi}{2} - \tau - \frac{\pi}{2}$ pulse sequence to the electron spin of the NV centres. The first $\frac{\pi}{2}$ pulse orientates the spin from $| 0 \rangle$ to a superposition state. This state evolves over a time τ , generating a phase difference between itself and $| 0 \rangle$. This phase difference is measured by applying the second $\frac{\pi}{2}$ pulse which orientates the spin back to its original axis. The phase difference is converted into population. These are detected by the ODMR method.

By increasing τ and maximising the phase difference, the sensitivity is improved. T_2^* is also involved in this sequence as this quantity randomises the phase difference during τ which results in the loss of contrast. To achieve peak contrast and sensitivity gain, the optimised situation is $\tau = T_2^*$ [3] [8] [13].

4.3 Photo-current Detected Magnetic Resonance

Photo-current detected magnetic resonance or PDMR is a different way of reading out NV electron spins. Instead of optical detection of the fluorescence intensity of the NV defect, the photo-current generated by two-photon excited electrons in the conduction band is measured. This means the setup only has to consist out of a laser and components to focus this light on the sample. An APD and filters are not necessary anymore. The readout is done via the electrodes on the sample, as seen in figure 8. The PDMR configuration results in a decrease in overall size of the setup.

Comparable to ODMR, the electrons are optically excited to the excited 3E state. Excited electrons either relax back to the ground state or are optically excited again. The electrons relaxing back emit fluorescent light, which can be used for simultaneous ODMR readout. The electrons that are excited again are sent to the conduction band and can be used for PDMR readout. This happens due to an underlying two-photon absorption process. By losing an electron to the conduction band, the NV centre becomes neutral (NV^0). It gets an electron back from either the bulk of the diamond or from another two-photon absorption process [18].

Like ODMR, if the electron first gets excited to the $| -1 \rangle$ or $| +1 \rangle$ ground state and then to the 3E excited state, then the electron has a bigger chance to decay via the metastable states. This meant a decrease in photo luminescence when measuring ODMR. In PDMR this also means a decrease, but now in photo-current. A visualisation of the process is shown in figure 7. Unlike ODMR, PDMR is not limited by saturation of the amount of excited electrons. This implies there should be a higher contrast possible with PDMR.

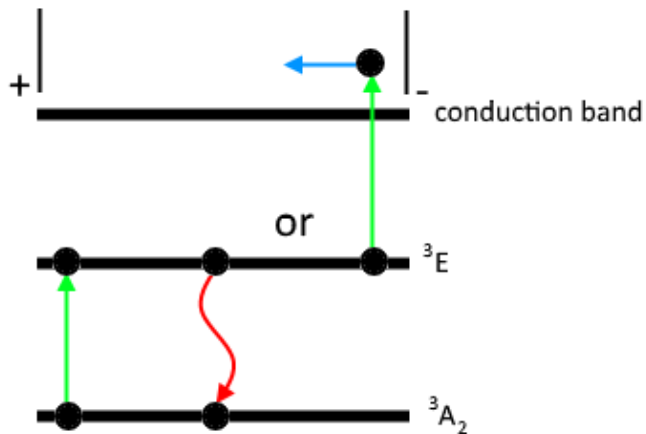


Figure 7: Comparison of the processes behind ODMR and PDMR. The green arrows indicate excitation. The red arrow shows the relaxation by emitting fluorescent light and the blue arrow is the electron which gets syphoned off of the diamond.

5 Magnetometry: the Development

5.1 Development of the ODMR Magnetometer: Part 1

One of the requirements for the BEXUS project is that the magnetometer device needs to be compact and lightweight. A schematic view of the setup with all the specifications of the parts used is given in appendix 10.1.

The laser used to raise the electrons to the excited triplet is a 50 mW, 520 nm (L520P50, 5,6 mm) laser diode mounted on a TCCLDM9 - Thermoelectric-Cooled Mount. The laser is controlled by a T-Cube Laser Diode Driver TLD001. This driver can regulate either the current or the power of the laser.

When leaving the source, the laser light first gets collimated by a 7,5 mm lens with a focal length of 20 mm (AC080-020-A-ML). Next, a lens with a clear aperture of 5 mm and a focal length of 15,29 mm (A260TM-A) is used to focus the laser light on the sample.

The sample is placed in the focus of the second lens, to get the highest intensity of fluorescent light (higher contrast). To get the electrons to the $m_s = +1$ or $m_s = -1$ ground states, resonant microwave frequencies have to be applied. In the proximity of an unknown magnetic field, these resonant frequencies are not known. Therefore a microwave sweep has to be applied in the relevant frequency range. In figure 8 the sample mount is shown. The golden electrodes marked with 'MW' are for the implementation of the microwaves on the sample. The ones marked with 'PD' are for PDMR. The sample can be seen at the crossroads of the electrodes.

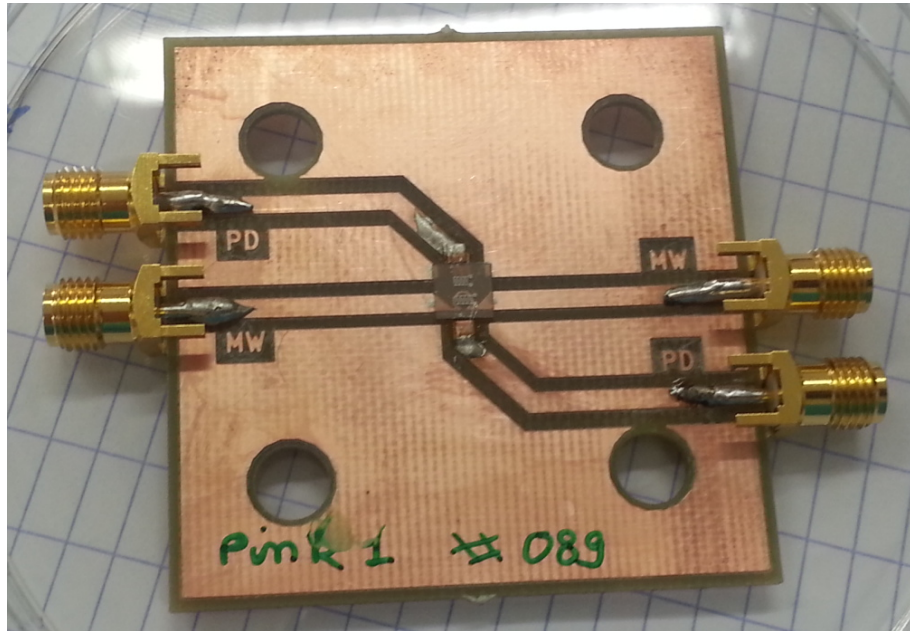


Figure 8: The component used to mount the sample. Contacts to apply the microwaves are indicated with 'MW'. Contacts for PDMR purposes are indicated with 'PD'.

The sample is prepared by electron irradiation and annealing of a type Ib diamond. Type Ib diamonds contain up to 500 ppm (parts per million) of single substituent nitrogen atoms.

The microwaves are generated by a SynthNV 34MHz - 4.4GHz RF Signal Generator, which is connected to one of the two electrodes. A terminator is connected to the second electrode. This terminator serves to prevent the microwaves to reflect back to the sample. The signal generator is controlled by an Arduino Mega ADK. This allows the frequency range and frequency intervals to be changed easily. A short summary of the used code is given further down this section.

The diverging fluorescent light leaving the sample will be collected by the next lens, with a clear aperture of 5 mm and a focal length of 4,51 mm (C230TMD-B). This light is collimated and is sent to a set of filters. The purpose of these filters is to filter out the unwanted wavelengths and to attenuate the intensity of the wanted wavelength. Attenuating is necessary as the APD has a maximum input power of 1 mW.

All filters have a diameter of 25 mm. The first filter has a cut-off wavelength at 800 nm (FESH0800). This one is used as a low-pass filter, to eliminate all the light with a wavelength higher than 800 nm. The second filter has a cut-on at 650 nm (FELH0650). Acting as a high-pass filter, it will cut off all the light with wavelengths beneath 650 nm. The third and fourth filters have a cut-on wavelength of 550 nm (FELH0550). These are for filtering out the green light coming from the laser. Two of them are necessary due to the high intensity of the light. Combining all these filters leaves a window from 650 to 800 nm, which corresponds to the emission window shown in figure 2. The final filter is a neutral density filter (ND10A) with an optical density of 1 (attenuation of factor 10) to attenuate the light so it does not damage the APD while still getting to the power of the laser for maximum contrast.

After passing through the filters, a final lens will focus the light on the APD. This lens has a clear aperture of 5,6 mm and a focal length of 15 mm (AC064-015-A-ML). The APD will convert the incoming intensity to an output voltage ranging from 0 V to 1,5 V, depending on how strong the fluorescence is. The APD itself is a silicon based photo detector (APD130A2/M) with an active area of 1 mm. This one is chosen for having a high responsivity in the relevant wavelength range (200-1000 nm).

The readout of the output signal of the APD is done by previously mentioned Arduino. This signal first needs to be converted from 0 V - 1,5 V to 0 V - 5 V, as the Arduino readout operates in this range. The way this is done is elaborated further down this section. The Arduino converts the 0 V - 5 V to a value between 0 and 1023, depending on the voltage. This data is then sent to a computer, which will then be processed by a LabVIEW program.

To deliver power to the optical setup, a compact electronic circuit is built, as seen in figure 9. As input power two 12 V batteries are used. The magnetometer needs +/- 12 V to power the APD, 5 V for the Arduino. The laser diode controller and laser need 5 V and +/- 15 V supply voltage. An amplification circuit is used to amplify the 0 V - 1,5 V APD output to 0 V - 5 V, in order to match full resolution of the Arduino ADC (Analog Digital Converter) input. The voltage conversions are done by Traco DC/DC converter units.

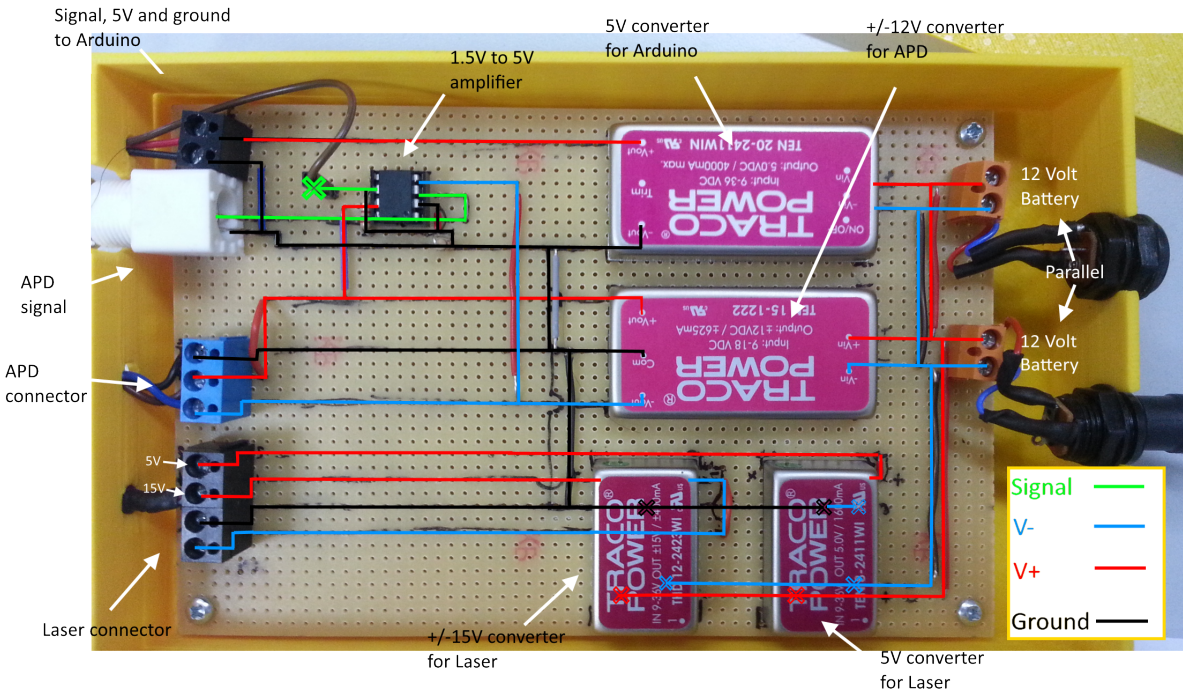
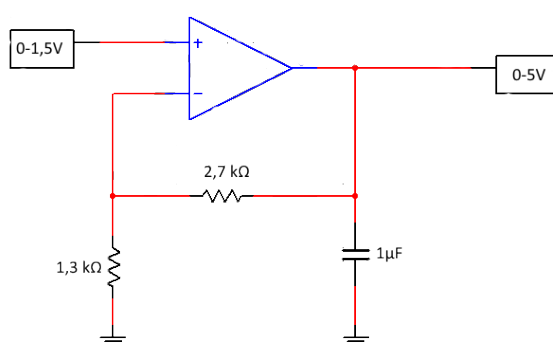
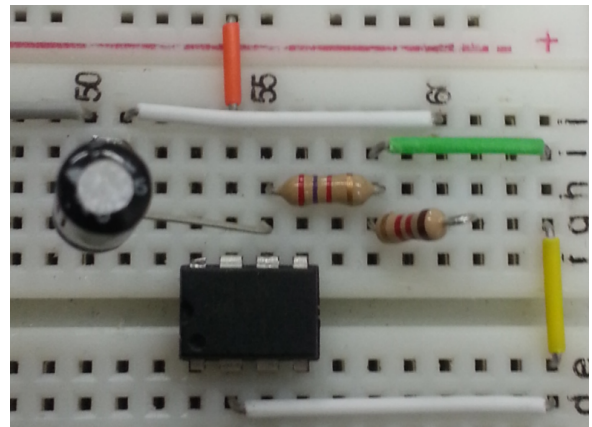


Figure 9: Conversion used to power the magnetometer and convert the signal. In green the signal coming from the APD and going to the Arduino for readout. In black the ground, in red the relative positive voltage and in blue the relative negative voltage.

The black screw terminals in figure 9 are the outputs going to the laser connector: 5 V, +/- 15 V and ground. The blue screw terminals are going to the APD input: ground and +/- 12 V. The white BNC connector is used as input for the APD output. This output is amplified by the amplifier circuit. A schematic is shown in figure 10a and 10b.



(a)



(b)

Figure 10: Amplification circuit used to amplify the 0 - 1,5 V APD output signal to a 0 - 5 V signal for the Arduino ADC input.

Both the readout of the APD and the microwave generator control is done by an Arduino Mega ADK. Arduino is used as it is inexpensive, compact and easy to use. An Arduino board is a compact and reliable micro-controller unit with a user-friendly programming environment.

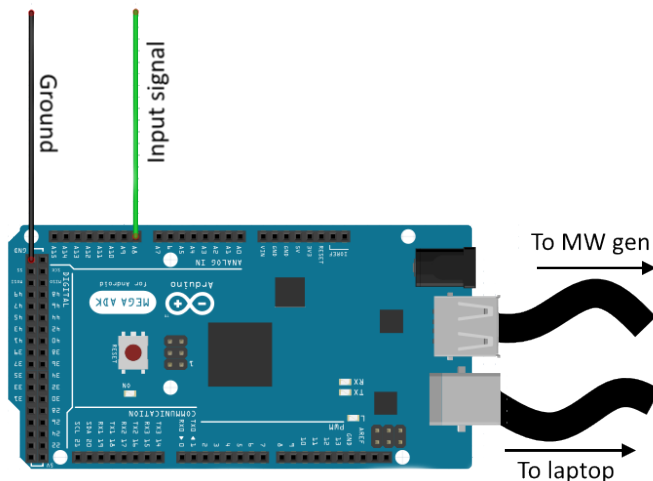


Figure 11: Simple setup of the used Arduino. The green wire indicates the output signal coming from the APD. The Arduino is powered by the USB connection to the laptop.

A short summary of the main testing code used to do the operations: Initially the parameters are given: the frequency range for the sweep and the step size of the frequencies. The readout pin on the Arduino is also defined (in this case it will be pin A8). The Arduino board will send the frequencies, which have to be applied to the sample, to the microwave generator. The frequencies will start from the lower bound in steps of the given step size. This will go on until reaching the upper bound. At every frequency the Arduino will read out the input of input pin A8. This data will be sent to a laptop in a certain string format to be processed. The format will have the form "frequency \tab intensity". The frequency will be given in MHz and the intensity will be a value between 0 and 1023 (depending on the voltage). For example "2870 \tab 985.0". The source code, with comments, is given in appendix 10.2 as well as the used libraries.

The program used to collect and process the data is made in LabVIEW. It first reads the incoming data from the USB port. When the data comes in, it will first be checked if it has the right format. If this is not the case it will be given an intensity of 0 for the frequency where the error occurs. This way it

will be clear this was an error when looking at the data afterwards. If the string has the right format it will be sent on to the next step where it will be split up into substrings. The first substring will contain the frequency while second one will contain the intensity. All the data will be put in a data array and is saved. The data is fitted and the parameters are calculated. The results will be visualised as a graph and the magnetic field strength will be calculated from the parameters.

A representative sweep of this setup can be seen in figure 12. This sweeps shows the effect of the magnetic field of the Earth on the frequency spectrum.

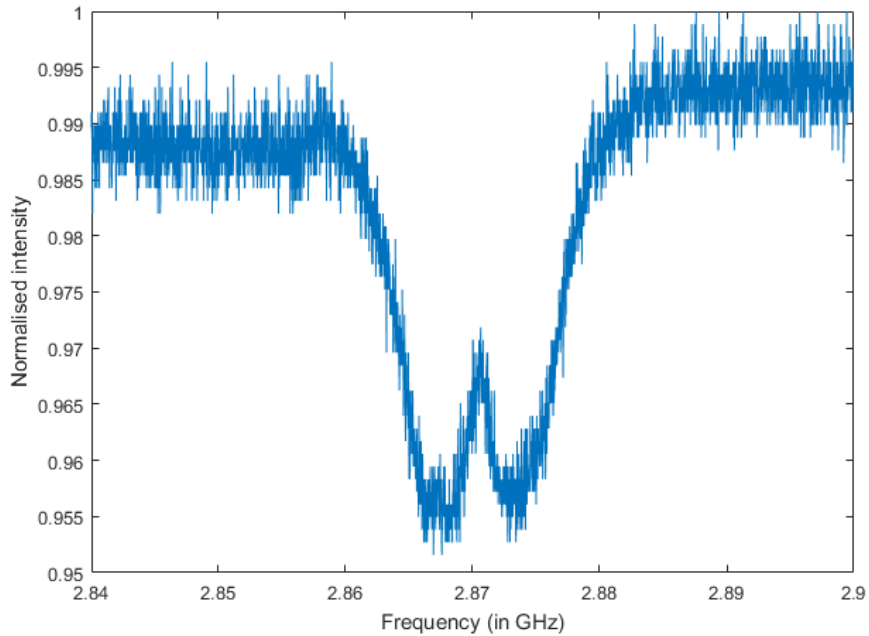


Figure 12: Representative ODMR sweep obtained by using the previously explained setup.

The fitting is done in the LabVIEW program by using a profile of two Lorentzians as shown in figure 13. Two Lorentzians were chosen (instead of more) due to figure 12 only showing two peaks. The function has the form

$$(4) \quad I(F) = A - \frac{BD^2}{(F - G - E)^2 + D^2} - \frac{CD^2}{(F - G + E)^2 + D^2}$$

A through E and G are the parameters derived from the fitting done by the LabVIEW program. A gives the offset of the intensity at non-resonant frequencies, B and C are the contrasts of the left and right peak, respectively. D gives the full-width at half maximum (FWHM), E is the splitting of the peaks relative to the zero-field splitting frequency, which is given by parameter G. F is the frequency which is applied to the sample. From parameter E the magnetic field can be recalculated by

$$(5) \quad B = \frac{E}{g_e \mu_b}$$

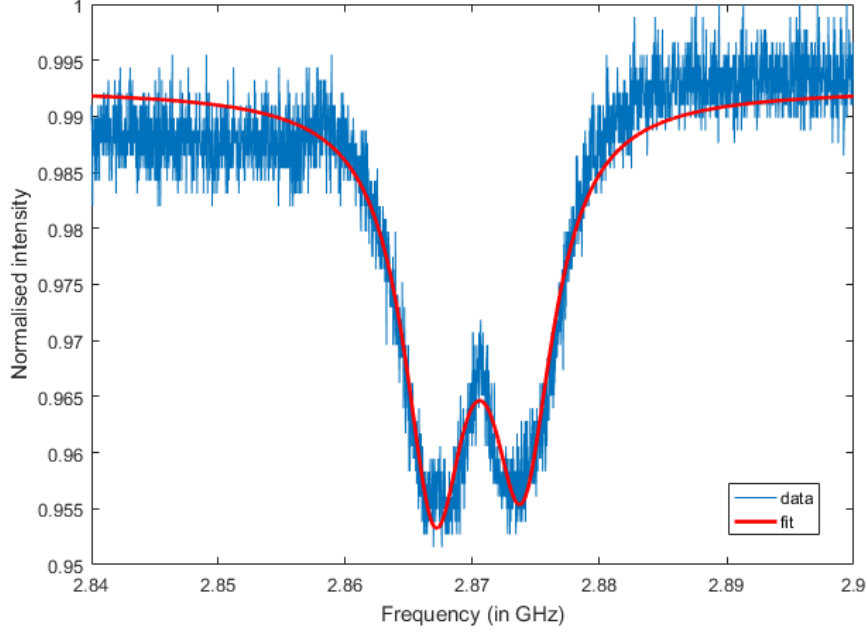


Figure 13: Representative ODMR sweep obtained by using the previously explained setup. In red a fit can be seen. This is obtained by making use of two Lorentzian profiles.

From the fitted data of figure 13 a splitting parameter E is found with a value of 3,435 MHz. Via equation 5 the magnetic field strength becomes 12267,8 nT. Earth's magnetic field has a vertical component of around $45 \mu\text{T}$ and a horizontal component of around $20 \mu\text{T}$ at the location where these measurements were done [25].

As mentioned in section 3.1 there are four sets of peaks corresponding to all the possible NV axes directions. Therefore, there should be more than just two peaks as seen in 12. Either the magnetometer is pointed in a direction so that Earth's magnetic field has the same effect on every NV axes direction. This also means Earth's magnetic field only has a component pointing straight up which means no matter how the magnetometer is rotated, it will always show the same splitting. As seen in figure 19 this is not the case.

This implies the peaks are overlapping. The fit will consider it as one set of peaks. This setup is able to detect magnetic field changes, but the sweep has to be more precise to be able to differentiate the different peaks. The fit will also have to be altered to fit eight peaks and not only two.

5.2 Development of the ODMR Magnetometer: Part 2

To get rid of most of the noise and resolve the peaks a lock-in amplifier is included in the setup.

Lock-in amplifiers are used to detect and measure small signals. Even when the signal is not visible due to noise, measurements of this signal are still possible by the lock-in amplifier. The noise may even be a thousand times larger. Lock-in amplifiers use phase-sensitive detection to single out the component of the signal at a specific reference frequency and phase (by mixing the reference and the input signal). Typically an experiment is excited at a fixed frequency and the lock-in detects the response from the experiment at the reference frequency. Noise signals, at frequencies other than the reference frequency, are rejected and do not affect the measurement.

Here the reference frequency is applied to both the lock-in amplifier and a microwave switch. This way the detection via the lock-in will only happen when the microwaves are being applied to the sample and the noise will be greatly reduced. The microwave switch is placed between the microwave generator and the sample. The one used is the Minicircuits ZASWA-2-50DR+ High Isolation Switch. This switch needs a ± 5 V supply voltage to operate. The converter in the previous section will be altered to do this task. The lock-in amplifier is a SR830 Lock-In Amplifier from Stanford Research Systems. The reference signal is applied by a function generator.

The time constant (τ_{lockin}) is an important parameter of the lock-in amplifier. The last step of the lock-in amplifier is the low-pass filter. The purpose of the low-pass filter is to attenuate signals going into the filter. The time constant is inversely proportional to the cutoff frequency. The higher it is, the narrower the frequency band that is allowed through the filter. For a given τ_{lockin} , the higher the frequency fed into the filter, the more it is attenuated. If all time varying signals are completely attenuated, only the DC component that comes out of the mixer will end up in the final output.

A representative sweep including the microwave switch and the lock-in amplifier is shown in figure 14.

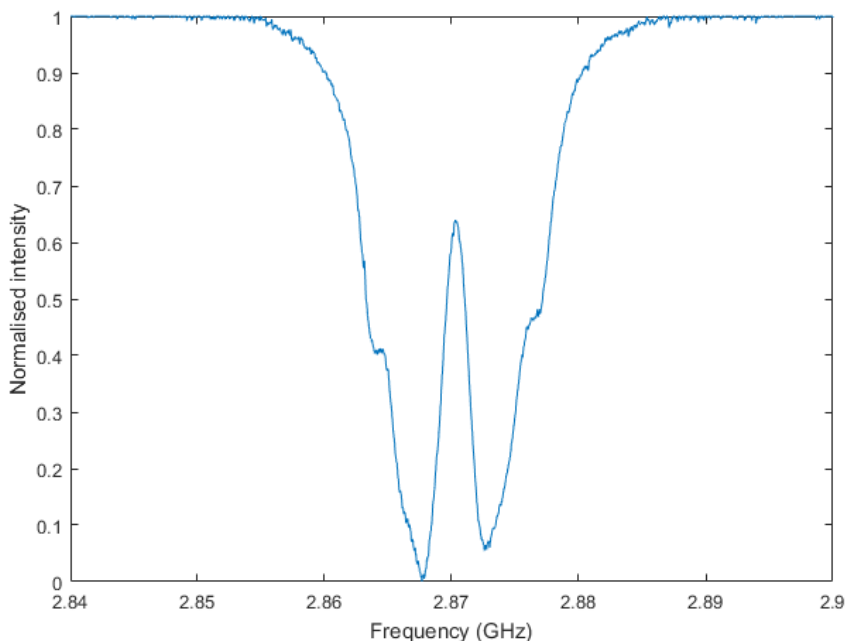


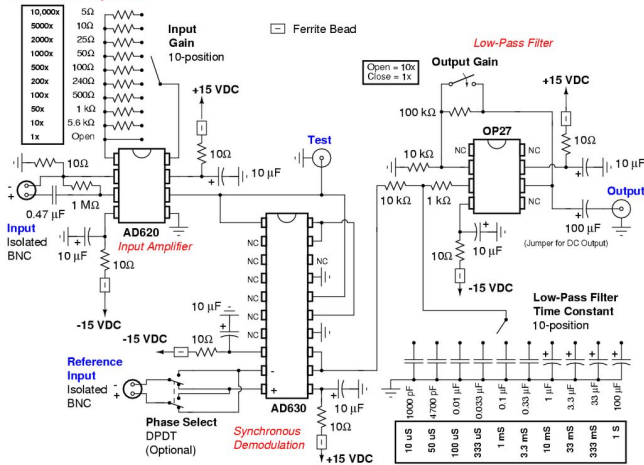
Figure 14: Representative sweep including the lock-in amplifier and the microwave switch. Magnetic field strength is that of the Earth.

In order to keep the setup as compact as possible, the previously mentioned function generator and the lock-in amplifier are not used. In the next stage of development the reference signal will be generated by the Arduino. The lock-in amplifier will be replaced by a self-made prototype much smaller in size. The schematics for the lock-in amplifier are shown in figure 15a.

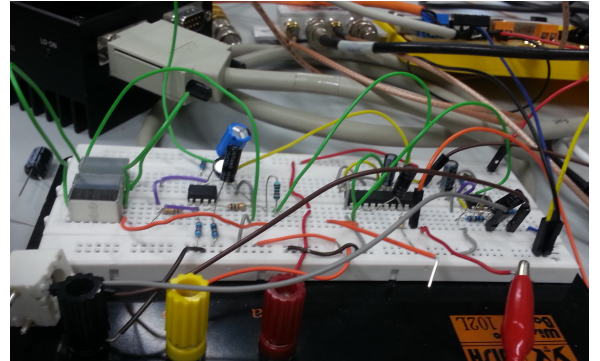
The lock-in amplifier can be seen as 3 major parts: an input amplifier, a synchronous demodulator and a low-pass filter/amplifier. The input amplifier amplifies the input signal from the APD using a variable gain resistor. The initial resistor used is a $5,6\text{ k}\Omega$ one. This gives a gain of 10. The amplifier used is an AD620 Instrumentation Amplifier. The synchronous demodulator (AD630 Balanced Modulator/Demodulator) is the component where the reference and input signal mixing happens. The low-pass filter and amplifier filters out the noise from the signal coming from the previous step and amplifiers the final signal. The used component is an OP27 Low Noise, Precision Operational Amplifier. This is where the time constant of the lock-in amplifier plays an important role.

The first version of the self-made lock-in amplifier can be seen in figure 15b. To power the lock-in amplifier the DC/DC power converters mentioned in the previous section are used. The next step in the development of the lock-in amplifier is the design and development of a printed circuit board (PCB).

Lock-In Amplifier



(a)



(b)

Figure 15: (a) Schematic of the lock-in amplifier [22]. (b) Setup of the self-made lock-in amplifier.

To optimise the lock-in amplifier for ODMR purposes, different time constants are tested. This is first tested with an input amplification 10. After finding the best time constant, the input gain is also optimised. In figure 16 the results are shown for different time constants. A reference frequency of 1,5 KHz (TTL) gives the best results. The splitting shown in the graphs is due to the presence of an external magnetic field produced by a disc magnet. Eight peaks can be seen each split in three more peaks. This effect is observable due to the hyperfine splitting effects.

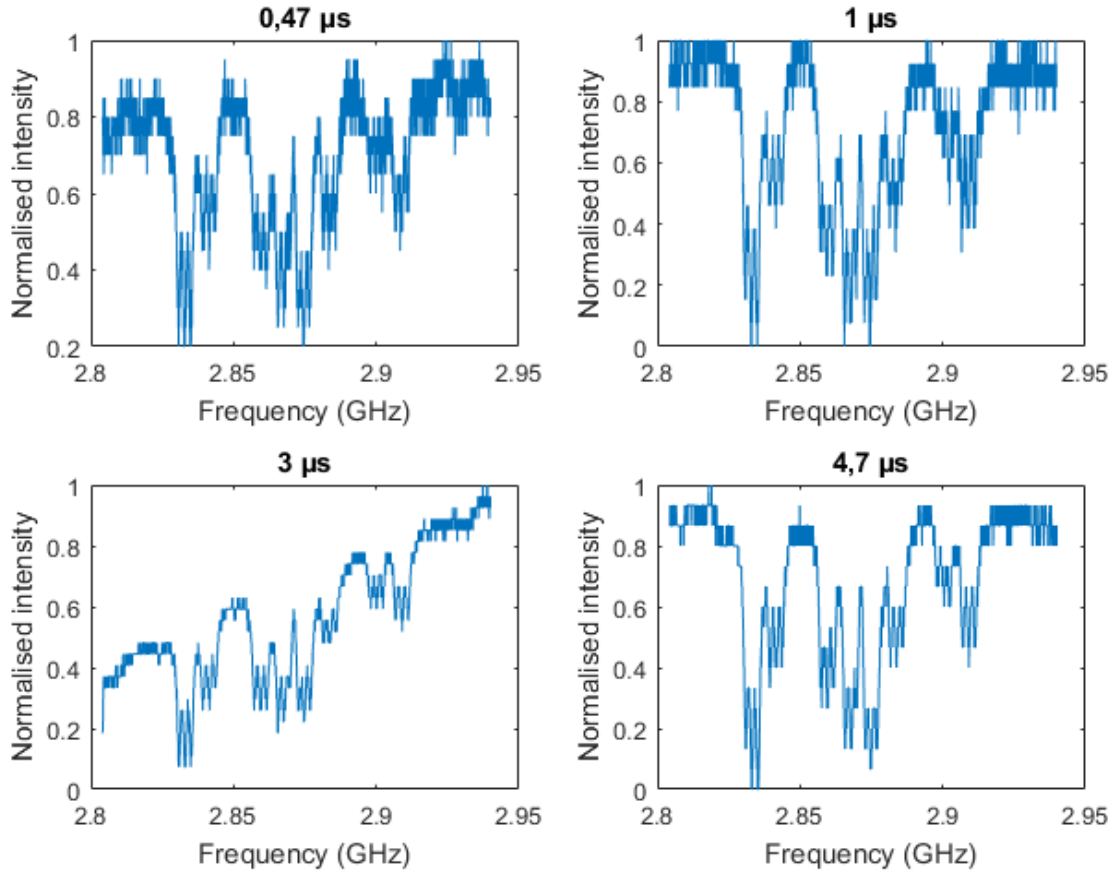


Figure 16: Sweeps at different time constants of the lock-in amplifier. Sweeps are taken in the presence of a disc magnet of unknown strength.

If the time constant is too low, the signal is lost in the noise. If the time constant is too high the signal is lost because the cut-off frequency is too low. The best time constant is at 3 μ s. This minimises the noise while keeping the details of the peaks in the signal.

With this time constant, different input gains are tested. The results are shown in figure 17. Resistors with values 680 Ω , 820 Ω , 1,2 k Ω and 5,6 k Ω are chosen. These correspond to gains of \sim 80, \sim 70, \sim 50 and 10, respectively. For a 3 μ s time constant, the best result is reached while using the 1,2 k Ω resistor. Lower resistances give a noisier final signal, while higher resistances give lower contrast.

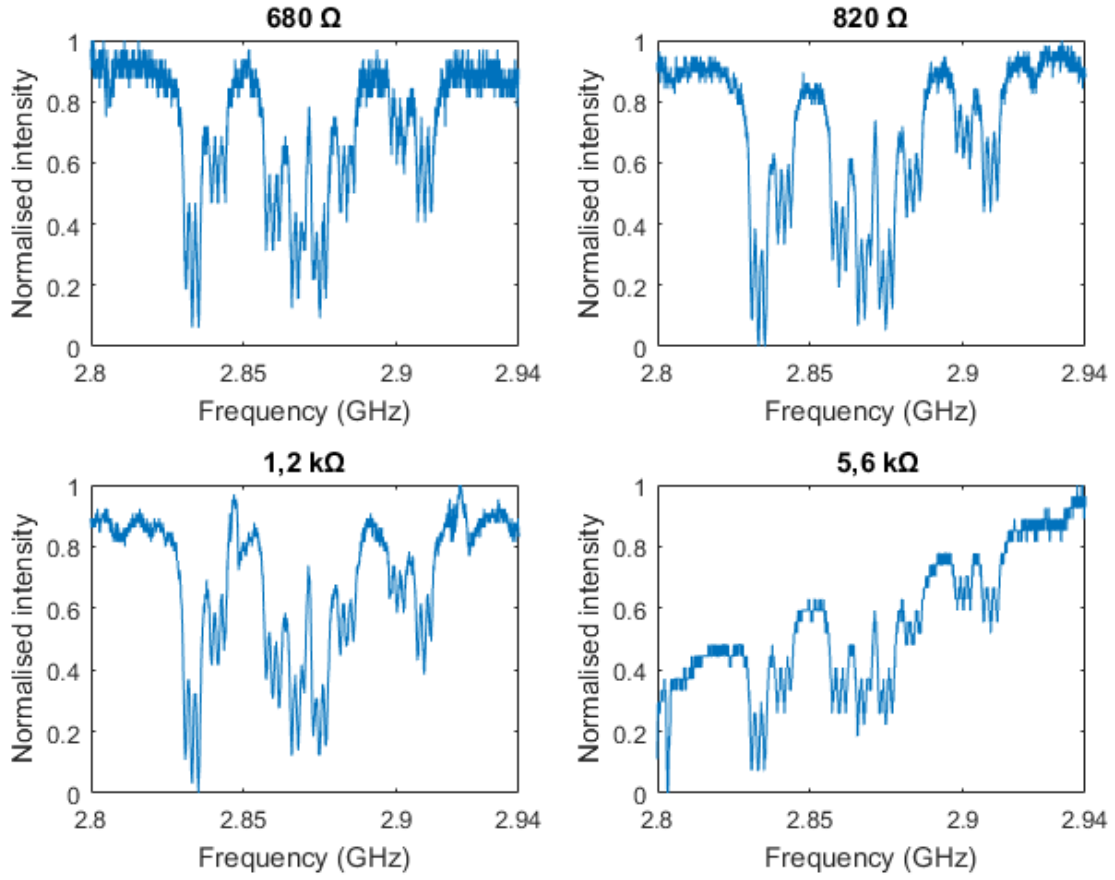


Figure 17: Sweeps at different input gains. A time constant of $3 \mu\text{s}$ and a reference frequency of $1,5 \text{ kHz}$ (sine). Measurements done in the neighbourhood of a disc magnet of unknown strength.

These optimised parameters will be used in the development of the compact PCB of the lock-in amplifier. The breadboard prototype of self-made lock-in amplifier showed low system stability due to poor quality of interconnections. It is expected that the PCB version will be more reliable and will give a better sweep.

5.3 Development of the PDMR Magnetometer

To measure a magnetic field by the PDMR method, a voltage source and a current preamplifier have to be added to the setup. The voltage source is used to move the electrons from the conduction band of the NV defect diamond to the current preamplifier. The preamplifier is used to buffer the input and amplify the signal to levels that can be used for further amplification. The currents created by the electrons in the conduction band are in the order of nanoamperes, therefore the amplification is necessary. A scheme of the PDMR setup can be seen in figure 18.

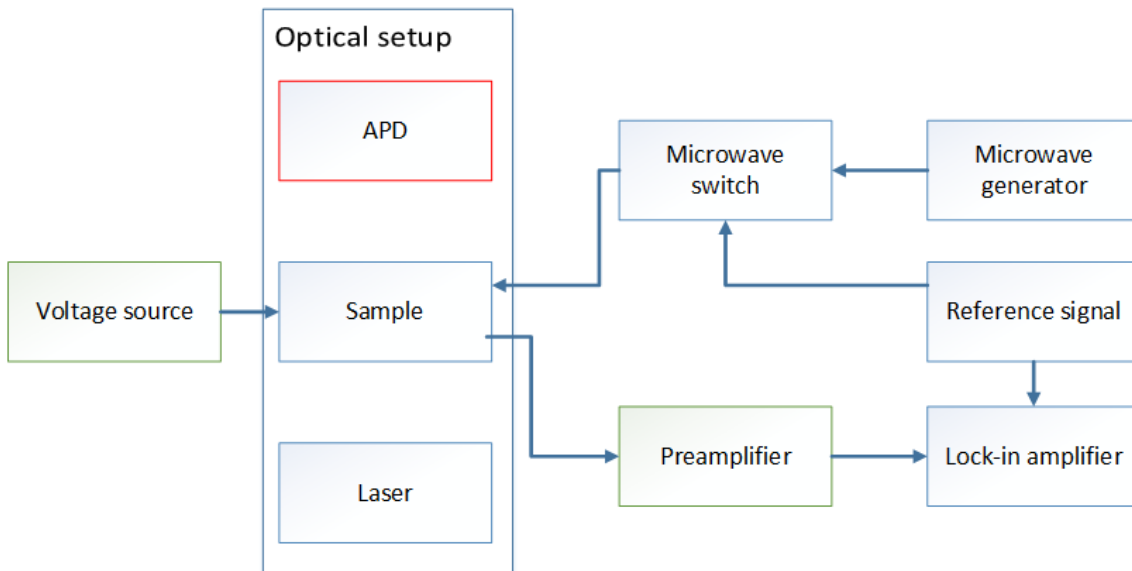


Figure 18: Scheme of the PDMR setup. In green the components added to the ODMR setup. In red the components not used in this setup.

The green laser is focused on the sample by the same components as in section 5.1. Similarly to the procedure shown in section 5.2, the microwaves are applied according to the reference signal. Electrons are excited to the conduction band. The voltage source moves the electrons to the next step which is the preamplifier, generating a small current. The current is amplified and detected by the lock-in amplifier.

As a voltage source a Keithley 487 Ammeter is used. For the used sample, a voltage of 100 V is applied. In case of a too high voltage, there is potential risk of damaging the electrodes. The limit voltage is derived from the gap between the electrodes and is equivalent to 75 V per 15 μm of gap width between electrodes. The used preamplifier is a Stanford Research Systems SR570 Low-Noise Current Preamplifier.

No PDMR signal was obtained using this setup. Reasons for this can be the sample quality or the way the microwaves are applied in combination with a low microwave power. In section 6.3 PDMR measurements results are discussed which were performed on the confocal setup at the IMO in Diepenbeek.

6 Results and Discussion

6.1 ODMR Magnetometer: Part 1

As a first test the directional dependence of Earth's magnetic field was tested. The measurements are done in Abisko, Sweden. The magnetometer in Kiruna, Sweden showed an x-component (North) of 10650 nT, a y-component (East) of -90 nT and a z-component (zenith) of 51830 nT [23]. The magnetometer was placed standing upright.

As the z-component is significantly larger than the x- and y-component, the angle of the total magnetic field lies close to the z-axis (11°). As previously mentioned, a magnetic field with only a z-component will cause the peaks to have the same splitting. As this angle with the z-axis is small, it is not expected to see a big change in the relative splitting of the peaks. As an attempt to calculate the magnetic field strength of the four directions, the fit in section 5.1 can be used. The data together with the fits is shown in figure 19.

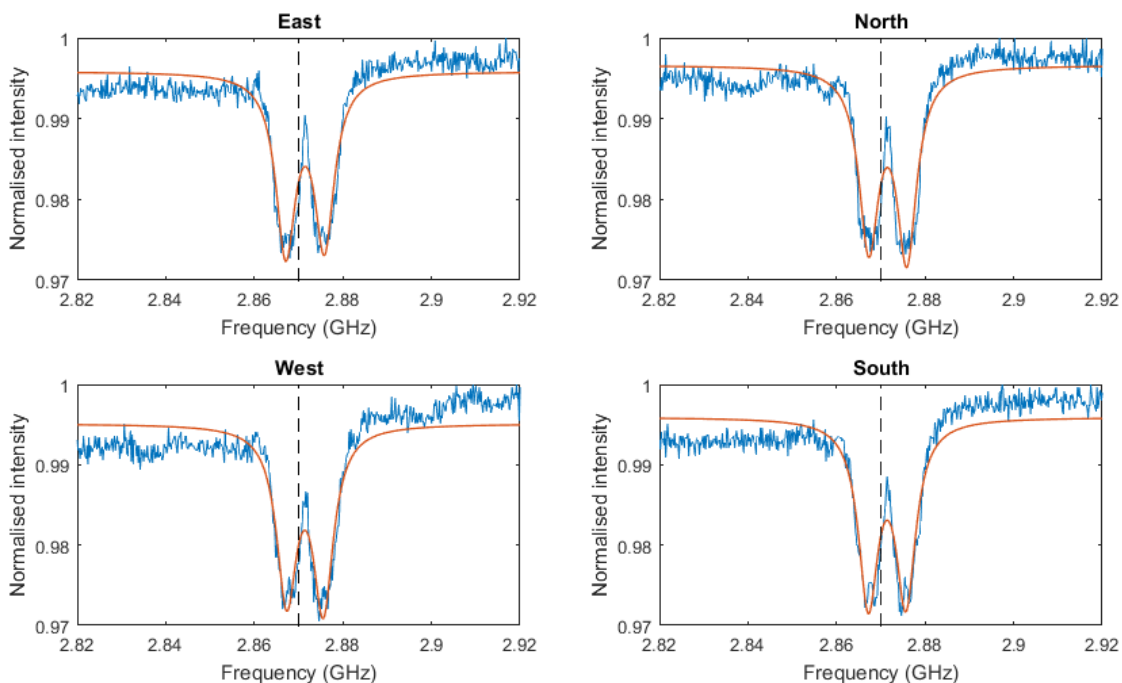


Figure 19: Microwave sweeps in four different directions: East, North, West and South. In blue the data, in red the fit. The black dotted line indicates the zero-field splitting of 2,87 GHz.

The resulting magnetic field strengths are 15627 nT in the eastern direction, 15356,3 nT in the northern direction, 14776,9 nT in the western direction and 15180,9 nT in the southern direction. A maximal change of $1 \mu\text{T}$ while rotating, which may have been caused by the fact that the magnetic field wasn't entirely pointed in the z-axis direction.

Notice the shift to right of the zero-field splitting frequency. This is due to the early algorithm used for smoothing done with Arduino. This should not be a problem as the peaks are still symmetric, but around a different frequency.

Attempting a measurement with an external DC magnetic field, a spectrum with too much noise was obtained. Therefore it was impossible to see any resonance frequencies. This was the main reason for the move to a lock-in amplifier.

6.2 ODMR Magnetometer: Part 2

By using a coil it is theoretically possible to apply a known magnetic field in a known direction. The coil is placed around the sample in order to create a magnetic with only a z-component at the sample's position. If the coil is longer than the sample's height, the field at the sample is nearly uniform. The strength of the magnetic field at the centre of the coil is approximated by

$$(6) \quad B = \frac{\mu NI}{L}$$

where μ is the permittivity in air, I is the applied current, N is the amount of windings and L is the length of the coil. N is chosen to be 30, L is 0,5 cm. Currents of 100, 200 and 300 mA are applied. In figure 20 the results can be seen.

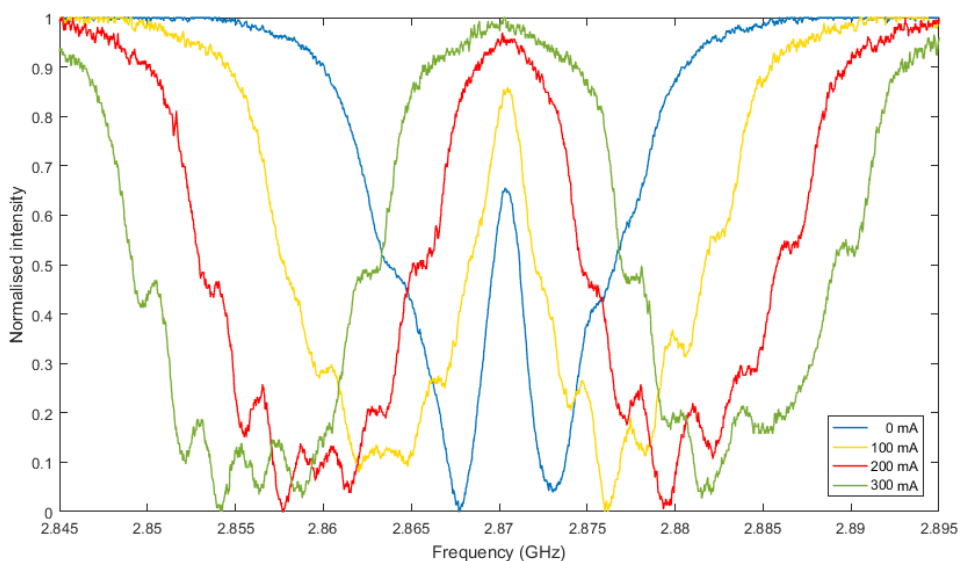


Figure 20: Set of microwave sweeps while in the presence of a magnetic field generating coil. The applied currents are 100, 200 and 300 mA.

As expected the splitting increases with an increasing current. Relative splitting of the peaks can also be seen. An explanation for this could be that the field isn't uniform at the sample, causing some NV axis directions to 'see' more of the magnetic field. Though, this does not explain the fact that there are more than eight peaks at currents of 200 and 300 mA. This last effect could be explained by pointing out that the sample is not infinitely small. The strength of the magnetic field decreases further away from the centre, as well as the uniformity. Which means the centre of the sample will sense a stronger and more uniform magnetic field than the borders of the sample.

One of the sweeps using the self-made lock-in amplifier from section 5.2 is shown in figure 21. The splitting is again caused by the presence of an external magnetic field produced by a disc magnet. The eight peaks are split up into three peaks each. When comparing the sweep to the structure shown in figure 22, it is clear that this is caused by hyperfine splitting. The model from section 3.4 can be further refined to include these effects. It is then possible to extract the hyperfine splitting parameters.

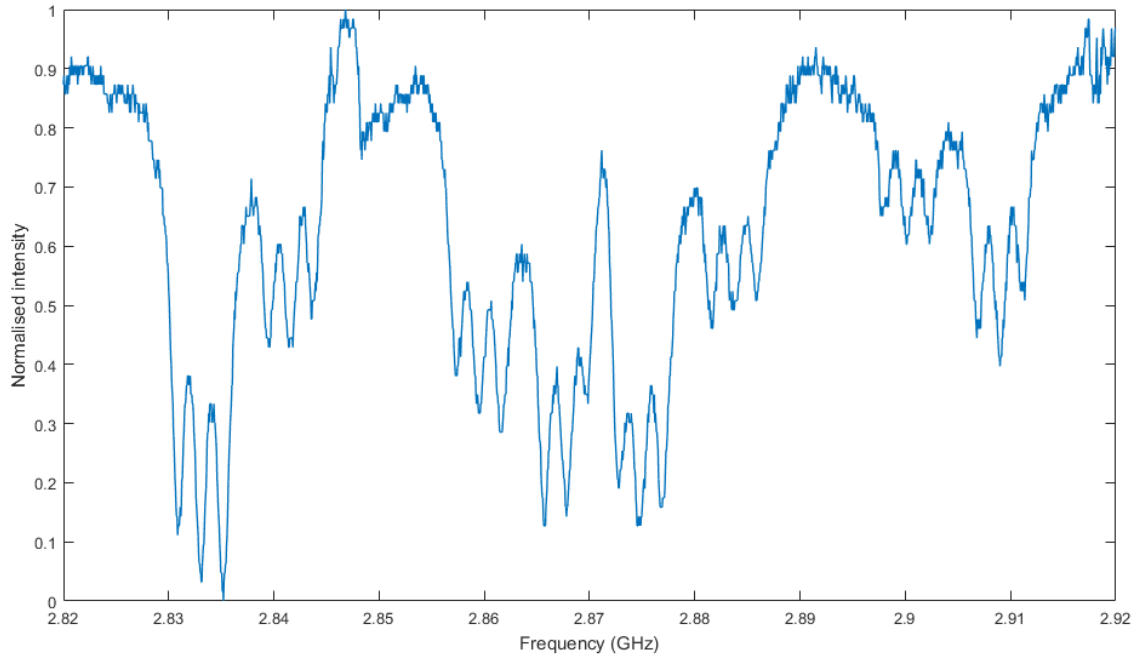


Figure 21: Frequency sweep showing hyperfine splitting caused by an external magnetic field produced by a disc magnet.

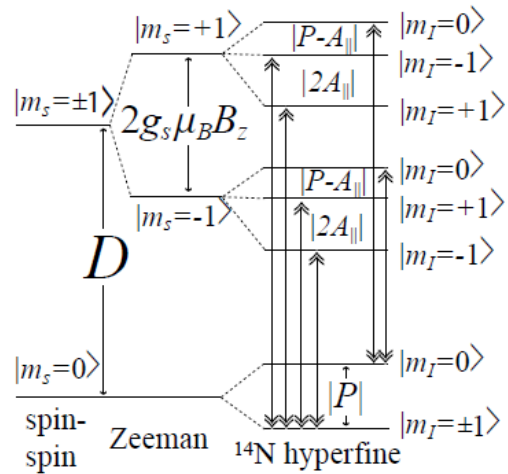


Figure 22: Structure of the NV defect while in the presence of an external magnetic field which causes there to be hyperfine splitting [4].

6.3 PDMR Magnetometer

As the PDMR setup for the prototype magnetometer did not deliver any signal, results from a set of measurements at the IMO setup are given. The measurements were done in the presence of an external DC magnetic field produced by a spherical magnet. The distance-dependent magnetic field strength of this magnet was measured and is shown in appendix 10.4. The magnet was placed at distances which correspond to $17 \mu\text{T}$, $26 \mu\text{T}$, $39 \mu\text{T}$ and $68 \mu\text{T}$. The results can be seen in figure 23.

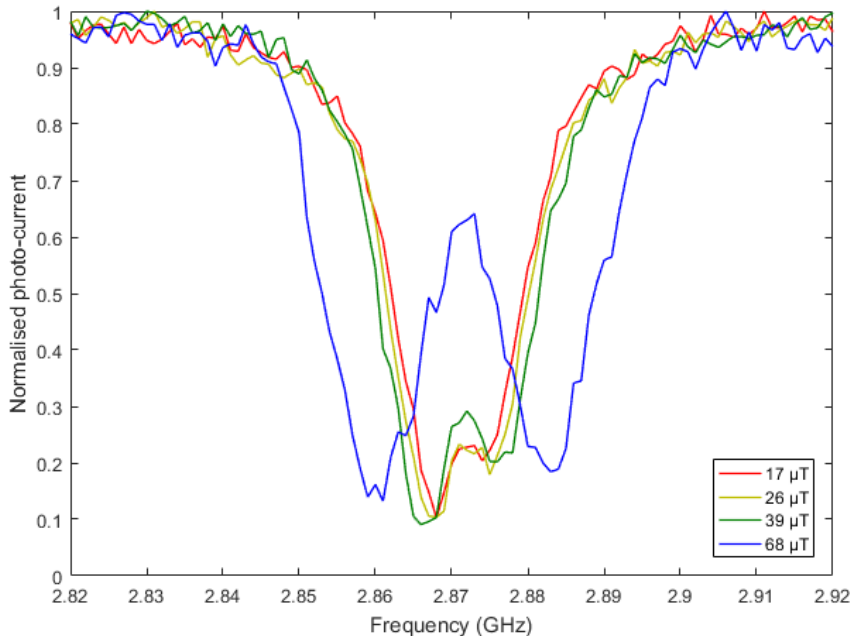


Figure 23: Set of PDMR measurements at magnetic field strengths of $17 \mu\text{T}$, $26 \mu\text{T}$, $39 \mu\text{T}$ and $68 \mu\text{T}$, performed at the setup at the IMO, Diepenbeek.

First of all, the splitting seems to increase linearly with a raising magnetic field strength. This corresponds to the theory. A visualisation of the linearity is given in figure 26 in appendix 10.3, as well as a fit. Using the fit from section 5.1 is not without problems.

As the direction of the spherical magnet was not known beforehand (only the strength in one direction) and the magnet does not have a uniform field, there is a very low chance the magnetic field direction at the diamond only has a z-component (which means all the sets of peaks have the same splitting). This means there should be more than two peaks visible. The cause for not seeing more peaks is the low step size of the frequencies. An attempt to fit the measurement at a magnetic field strength of $68 \mu\text{T}$ is shown in figure 24. The fit used is the same as in section 5.1 (for two peaks).

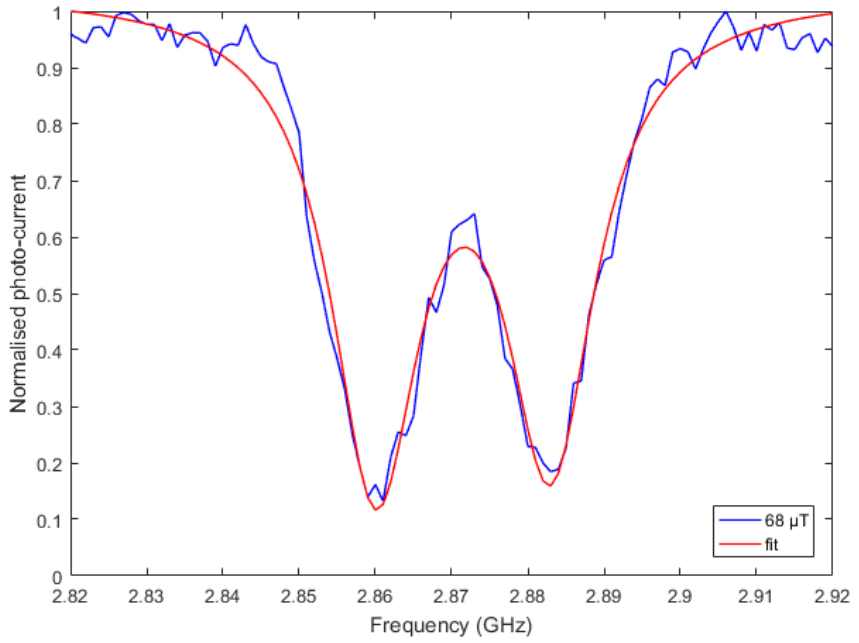


Figure 24: PD MR measurement at a magnetic field strength of $68 \mu\text{T}$. In red the fit of the data.

The parameters found from the fit are: the splitting is 11,4751 and a mean contrast of 79,84%. Recalculating the magnetic field strength via 5 gives a value of $40,98 \mu\text{T}$. This shows that the peaks need to be more resolved so a more appropriate fit can be utilised. This will also allow the determination of the direction of the magnetic field.

7 Conclusion and a Look Forward

A working, sensitive prototype magnetometer device based on NV defect diamonds has been developed. The first version of the ODMR-based magnetometer showed a change when exposed to an external magnetic field. At higher fields the obtained spectrum has too much noise which causes the peaks to be unresolvable.

Using a lock-in amplifier has shown to be a significant improvement for the obtained data. The peaks are more resolved and the noise is reduced. More information can be obtained from these measurements to define the direction and strength of the magnetic field. A self-made lock-in amplifier has been developed. The measurements obtained from using this lock-in amplifier are comparable to the professional one, while reducing the size significantly.

The PDMR method itself is still in an early phase of development and needs to be further explored prior to its application. The first task is to obtain a stable signal using the setup at the optical lab at the IMO. Pulse measurements, calibration and sensitivity measurements are also necessary for further development.

The magnetometer device needs more testing to be used in the BEXUS project. A better fit is necessary to determine the magnetic field strength and direction. This fit should consider a standard of eight peaks and even hyperfine splitting. A PCB version of the self-made lock-in amplifier will be developed to further refine the obtained data.

Calibration is still an important step in the process. With a uniform magnetic field and a suitable fit the diamond has to be calibrated in order to exactly calculate the strength and direction at every moment. Another important task is to determine and increase the sensitivity of the magnetometer. For the BEXUS project changes in the range of one nT are sufficient. If this cannot be reached, using the pulsing technique, mentioned in section 4.2, to get a bigger sensitivity is necessary.

As this project has to be limited in size, LabVIEW cannot be used. Therefore it is necessary to do the processing of the data on board. Other devices such as the laser driver can also be replaced by a self developed device to reduce the overall size and power consumption.

Test are necessary to see if extreme circumstances influence the results. The extensive testing of the system stability in different kinds of environments are to be done. The magnetometer will be tested in a climate chamber prior to the exposure of the cold temperature and cosmic radiation of outer space.

8 Acknowledgements

I want to express my gratitude to the amazing people of the Photonics Department at the IMO in Diepenbeek for welcoming me into a friendly atmosphere and for the support and guidance from start to finish. I'd like to thank the OSCAR-BEXUS team for involving me in such an exciting project, as well as giving me tons of advice. I'm looking forward to finish this project together with the team. I also want to express my gratitude to the X-LAB team at UHasselt for their help and support whenever I needed it. Finally, a big thank you to all the 3rd year Bachelor students who gave me advice and helped me throughout the last six months.

9 References

- [1] J. Clarke, A. I. Braginski, *The SQUID Handbook*, Wiley-VCH, Weinheim (2004).
- [2] C. Kittel, *Introduction to Solid State Physics*, Eight Edition (2005).
- [3] L. Rondin, J.-P. Tetienne, T. Hingant, J.-F. Roch, P. Maletinsky, V. Jacques, *Magnetometry with nitrogen-vacancy defects in diamond* (2014).
- [4] V. M. Acosta, *Optical Magnetometry with Nitrogen-Vacancy Centers in Diamond* (2011).
- [5] M. W. Doherty, N. B. Manson, P. Delaney, F. Jelezko, J. Wrachtrup, L. C.L. Hollenberg, *The nitrogen-vacancy colour centre in diamond* (2013).
- [6] M. Chipaux, A. Tallaire, J. Achard, S. Pezzagna, J. Meijer, V. Jacques, J.-F. Roch, T. Debuisschert, *Magnetic imaging with an ensemble of Nitrogen Vacancy centers in diamond* (2014).
- [7] N. B. Manson, J. P. Harrison, M.J. Sellars, *The nitrogen-vacancy center in diamond re-visited* (2006).
- [8] C. L. Degen, *Scanning magnetic field microscope with a diamond single-spin sensor* (2008).
- [9] M.W. Doherty, F. Dolde, H. Fedder, F. Jelezko, J. Wrachtrup, N.B. Manson, L.C.L. Hollenberg, *Theory of the ground state spin of the NV center in diamond: I. Fine structure, hyperfine structure, and interactions with electric, magnetic and strain fields* (2011).
- [10] J. R. Maze, A. Gali, E. Togan, Y Chu, A. Trifonov, E. Kaxiras, M. D. Lukin, *Properties of nitrogen-vacancy centers in diamond: the group theoretic approach* (2011).
- [11] J. R. Maze, P. L. Stanwix, J. S. Hodges, S. Hong, J. M. Taylor, P. Cappellaro, L. Jiang, M. V. Gurudev Dutt, E. Togan, A. S. Zibrov, A. Yacoby, R. L. Walsworth, M. D. Lukin, *Nanoscale magnetic sensing with an individual electronic spin in diamond* (2008).
- [12] F. Hilser, G. Burkard, *All-optical control of the spin state in the NV⁻ center in diamond* (2012).
- [13] H. J. Mamin, M. Kim, M. H. Sherwood, C. T. Rettner, K. Ohno, D. D. Awschalom, D. Rugar, *Nanoscale Nuclear Magnetic Resonance with a Nitrogen-Vacancy Spin Sensor* (2013).
- [14] T. Wolf, P. Neumann, K. Nakamura, H. Sumiya, J. Isoya, J. Wrachtrup, *A subpicotesla diamond magnetometer* (2015).
- [15] A. Dreau, M. Lesik, L. Rondin, P. Spinicelli, O. Arcizet, J.-F. Roch, and V. Jacques, *Avoiding power broadening in optically detected magnetic resonance of single NV defects for enhanced DC-magnetic field sensitivity* (2012).
- [16] R. Schirhagl, K. Chang, M. Loretz, C. L. Degen, *Nitrogen-Vacancy Centers in Diamond: Nanoscale Sensors for Physics and Biology* (2014).
- [17] J. H. N. Loubser, J. A. Van Wyk, *Electron spin resonance in the study of diamond* (1978).
- [18] E. Bourgeois, A. Jarmola, P. Siyushev, M. Gulka, J. Hruby, F. Jelezko, D. Budker, M. Nesladek, *Photoelectric detection of electron spin resonance of nitrogen-vacancy centres in diamond* (2015).
- [19] A. Lenef, S. C. Rand, *Electronic structure of the N-V center in diamond: Theory*
- [20] P. Neumann, R. Kolesov, V. Jacques, J. Beck, J. Tisler, A. Batalov, L. Rogers, N. B. Manson, G. Balasubramanian, F. Jelezko, J. Wrachtrup, *Excited-state spectroscopy of single NV defect in diamond using optically detected magnetic resonance*

- [21] Institute for Molecular Engineering, University of Chicago - Excited-State Spectroscopy Using Single Spin Manipulation, URL: <http://ime.uchicago.edu/awschalomlab/research/>
- [22] Instructables - Lock-in Amplifier, URL: <http://www.instructables.com/id/Lock-in-Amplifier>
- [23] Swedish Institute of Space Physics - Processed Kiruna Magnetogram (2016-03-06), URL: [http://www.irf.se/Observatory/?link\[Magnetometers\]=Data](http://www.irf.se/Observatory/?link[Magnetometers]=Data)
- [24] Wikimedia Commons - absorption/emission spectrum of N-V- center in diamond at 300K, URL: <https://commons.wikimedia.org/wiki/File:NVple.JPG>
- [25] British Geological Survey, Natural Environment Research Council - The Earth's Magnetic Field: An Overview, URL: http://www.geomag.bgs.ac.uk/education/earthmag.html#_Toc2075556

10 Appendices

10.1 Appendix A: Optical Setup with Specifications

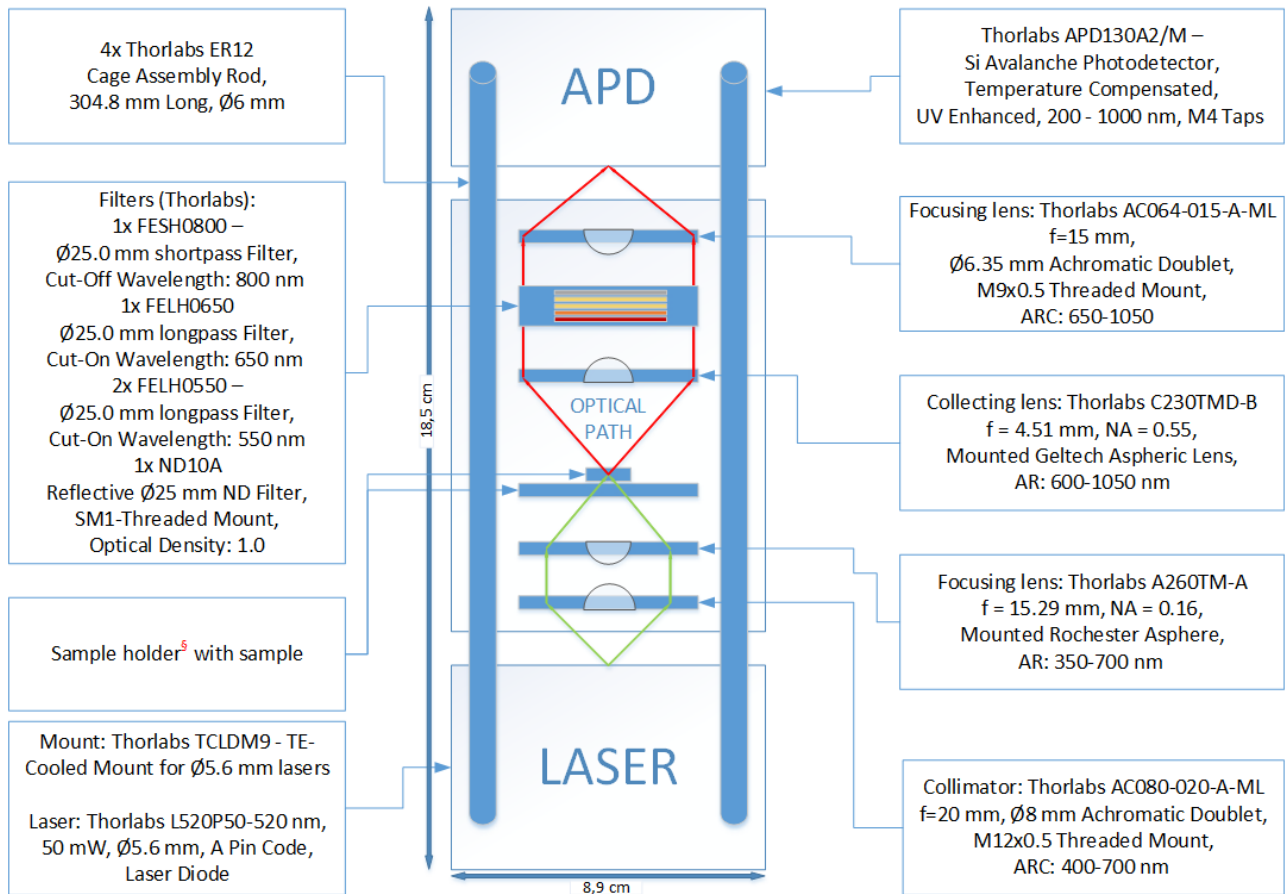


Figure 25: Optical setup of the magnetometer, with every used component. (§See figure 8)

10.2 Appendix B: Arduino Test Code

Libraries used:

- AndroidAccessory
- USB_Host_Shield_20
- CapacitiveSensor

```
// VARS AND CONSTANTS

int APD = A8;           // APD analog input
int n = 1;              // number of integrations
int nt = 0;             // integration delay
int readDelay = 0;

float startMW = 2820;   // MW start frequency
float endMW = 2920;    // MW stop frequency
float stepMW = 1;       // MW step size

int avg = 1;

float gyro = 28 * pow(10,-6); // e spin gyromagnetic ratio, to calculate the magnetic field

// USB libs.
#include <cdcacm.h>
#include <usbbhub.h>

#include "pgmstrings.h"

// Satisfy the IDE, which needs to see the include statement in the ino too.
#ifndef dobogusinclude
#include <spi4teensy3.h>
#include <SPI.h>
#endif

class ACMAsyncOper : public CDCAsyncOper
{
public:
    uint8_t OnInit(ACM *pacm);
};

uint8_t ACMAsyncOper::OnInit(ACM *pacm)
{
    uint8_t rcode;
//     Set DTR = 1 RTS=1
    rcode = pacm->SetControlLineState(3);

    if (rcode)
    {
        ErrorMessage<uint8_t>(PSTR("SetControlLineState"), rcode);
        return rcode;
    }

    LINE_CODING lc;
    lc.dwDTERate = 9600;
    lc.bCharFormat = 0;
    lc.bParityType = 0;
    lc.bDataBits = 8;

    rcode = pacm->SetLineCoding(&lc);

    if (rcode)
        ErrorMessage<uint8_t>(PSTR("SetLineCoding"), rcode);

    return rcode;
}

USB      Usb;
//USBBHub      Hub(&Usb);
ACMAsyncOper  AsyncOper;
ACM          Acm(&Usb, &AsyncOper);
```

```

// SETUP

void setup()
{
    Serial.begin( 115200 );
#if !defined(_MIPSEL_)
    while (!Serial); // Wait for serial port to connect
#endif

    if (Usb.Init() == -1)
        Serial.println("OSCOKIRQ failed to assert");

    delay( 200 );
}

// MAIN LOOP

void loop() {
    Usb.Task();

    if( Acm.isReady() ) {

        float frequency = startMW; //initialise starting frequency
        float intensity = 0;

        int var = 0;

        //start sweep loop
        while (frequency < endMW){ // as long as the frequency is smaller than the upper bound
            frequency = (startMW + (var*stepMW)); // set frequency
            String str ("f" + String(frequency)); // make command

            //send command to MW generator
            uint8_t rcode;

            int ln = str.length()+1;
            char strbuf[ln];
            str.toCharArray(strbuf,ln);
            rcode = Acm.SndData(strlen(strbuf), (uint8_t*)strbuf);
            if (rcode)
                ErrorMessage<uint8_t>(PSTR("SndData"), rcode);

            delay(10);
            var++;
            intensity = readAPD(); // Get readout from APD

            // serial output
            Serial.print(frequency,3);
            Serial.print("\t");
            Serial.print(intensity);
            Serial.print("+");

            if (Serial.available() > 0) { // Change stepMW through LabVIEW
                String input = Serial.readString();
                stepMW = analyzeString(input, stepMW);
            }

        }
        delay(75);
    }
}

float readAPD(){ // Get readout from APD

    float voltage = 0;
    voltage = voltage + analogRead(APD); //read APD analog input
    return voltage;
}

```

```
}

float analyzeString(String cmd, float frequency) { // Change stepMW through LabVIEW
// identify string and turn it into case number

float result = frequency;

int lng = cmd.length();
if (cmd.startsWith("freq")){
int index = cmd.indexOf("q") + 1;
cmd = cmd.substring(index,lng);
result = cmd.toFloat();
}

return result;

}
```

10.3 Appendix C: Linearity of the PDMR Measurements

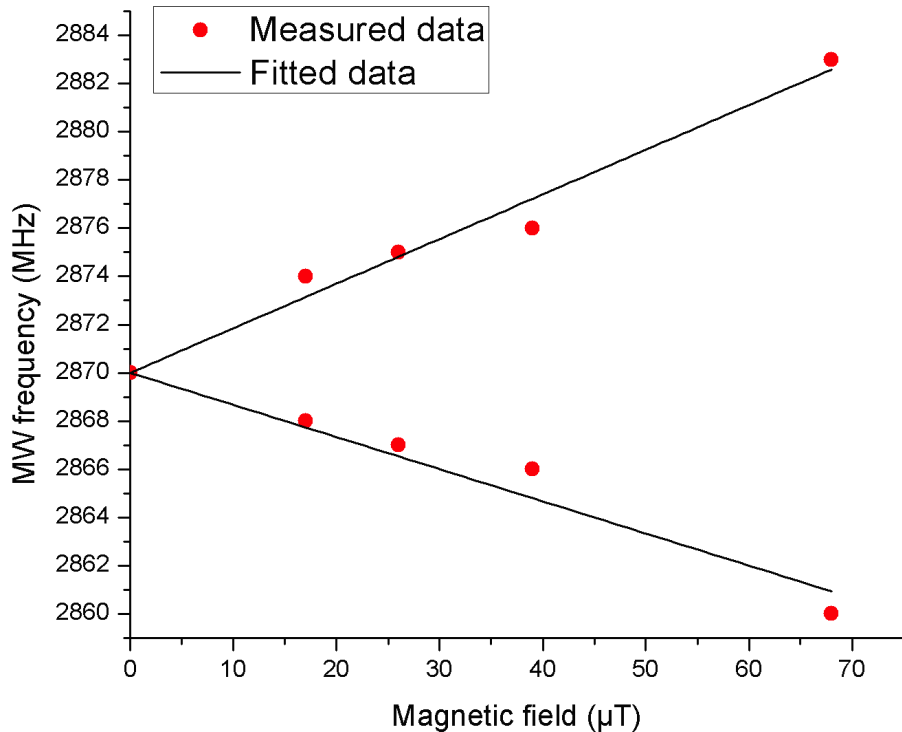


Figure 26: Linearity of the PDMR measurements at $17 \mu\text{T}$, $26 \mu\text{T}$, $39 \mu\text{T}$ and $68 \mu\text{T}$. The red dots indicate the minimum values of the peaks.

10.4 Appendix D: Magnetic Field Strength of the Spherical Magnet

Measurements were done with the Simple Aurora Monitor magnetometer system (SAM-III) in one of the three possible directions.

Distance (cm)	Average field (in nT)
2,5	68498,25
5	24757
7,5	8787,75
10	4279,75
12,5	2447,75
15	1498,25
17,5	999,75
20	705,75
22,5	501,25
25	371,5
27,5	281
30	221,25
32,5	164,25
35	123,5
37,5	106,25
40	91,75

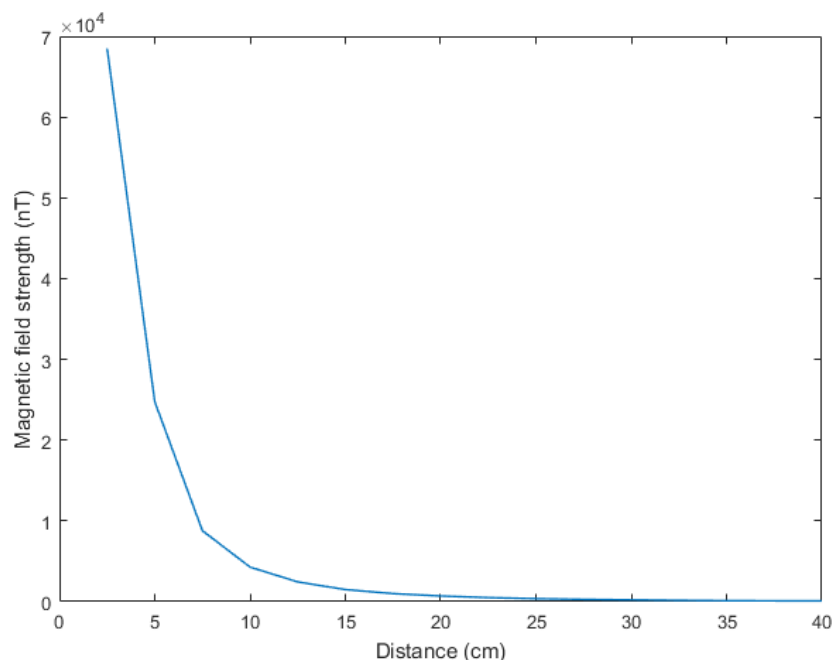


Figure 27: Graph of the values in the previous table.